Author's Accepted Manuscript

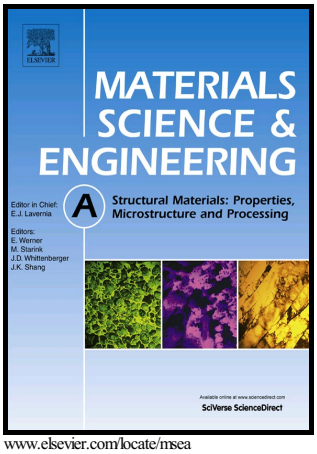

www.elsevier.com/locate/msea

Stress state-dependent mechanics of additively manufactured 304L stainless steel: Part 2 – characterization and modeling of macroscopic plasticity behavior

Zhuqing Wang, Allison M. Beese

PII: S0921-5093(18)31617-4
DOI: https://doi.org/10.1016/j.msea.2018.11.091
Reference: MSA37211

To appear in: *Materials Science & Engineering A*

Received date: 20 September 2018
Revised date: 17 November 2018
Accepted date: 19 November 2018

Cite this article as: Zhuqing Wang and Allison M. Beese, Stress state-dependent mechanics of additively manufactured 304L stainless steel: Part 2 – characterization and modeling of macroscopic plasticity behavior, *Materials Science & Engineering A,* https://doi.org/10.1016/j.msea.2018.11.091

Stress state-dependent mechanics of additively manufactured 304L stainless steel: Part 2 – characterization and modeling of macroscopic plasticity behavior

Zhuqing Wang[1] and Allison M. Beese[1,2*]

[1]Department of Materials Science and Engineering, Pennsylvania State University, University Park, PA 16802

[2]Department of Mechanical Engineering, Pennsylvania State University, University Park, PA 16802

*Corresponding author: amb961@psu.edu

Abstract

A model that describes macroscopic plasticity behavior of additively manufactured 304L stainless steel, in terms of its stress state-dependent microstructural austenite-to-α' martensite phase transformation is developed. Specifically, a stress state-, texture-, and chemistry-dependent strain-induced martensitic transformation kinetics equation was coupled to an isotropic hardening law in order to explicitly link the macroscopic strain hardening behavior in this material to its microstructural evolution. The plasticity model was implemented into a finite element code, calibrated using experimental data under uniaxial tension, uniaxial compression, pure shear, and validated using experimental data under combined tension and shear loading. The simulated results were in good agreement with the corresponding experimental data for all stress states studied for calibration and validation, demonstrating the predictiveness of the plasticity model developed.

Keywords:

Additive manufacturing; Iron alloys; Phase transformation; Plasticity; Finite element analysis

1. Introduction

Additive manufacturing (AM) can be used to fabricate near net-shaped 3-dimensional components layer-by-layer. Laser-, powder-based directed energy deposition (DED) AM of metals involves a repetitive process of the delivery of powder by nozzles to a location within a 2D layer of a 3D part, melting of the powder by a laser beam, rapid cooling of the melt pool, and fusion of the cooled material to the substrate or layer below [1–3]. Due to the complex thermal history in AM, the microstructures and mechanical properties of additively manufactured materials differ from those of their conventionally processed counterparts [4–11].

A key benefit of AM is its potential to fabricate complex shaped structural components [1,12]. However, when geometrically complex components are subjected to load, both the stress level and the stress state will be location dependent. While previous research has focused on understanding the mechanical behavior of additively manufactured materials subjected to uniaxial tension and compression [13–24], these uniaxial stress states are insufficient for describing how additively manufactured materials will perform under more realistic multiaxial stress states.

In this work, the multiaxial plasticity behavior of AISI type 304L austenitic stainless steel (SS304L) fabricated by DED AM was studied, and a plasticity model for this material is proposed. When plastically deformed, austenitic stainless steels have the potential to undergo a microstructural strain-induced phase transformation from a relatively soft face centered cubic (fcc) austenite to a relatively strong body centered cubic (bcc) α’ martensite, resulting in an increase in strain hardening on the macroscale [25–36]. The phase transformation kinetics are influenced by temperature, chemical composition, texture, stress state, strain, and strain rate [29,30,37,38].

Both micromechanical and phenomenological constitutive plasticity models have been developed for texture-free conventionally processed austenitic stainless steels undergoing strain-induced martensitic phase transformation [25,32,39–50] . Micromechanics-based models involve the modeling of the phase evolution due to martensitic transformation, and the prediction of the macroscopic constitutive behavior using homogenization methods varying from a simple rule of mixtures [25,42–45] to more advanced methods [32,46–49,51]. Hallberg et al. [44] proposed a micromechanical constitutive model for austenitic stainless steels, in which the yield surface is determined by using a nonlinear mixture rule to combine the yield stresses of austenite and α' martensite. Post et al. [45] proposed a model to describe the constitutive behavior of stainless steel with strain-induced martensitic transformation, in which the flow stresses of austenite and martensite are determined by dislocation density, phase fraction, and plastic strain, and the macroscopic flow stress is computed by combining the flow stresses of the two phases using a nonlinear rule of mixtures. In a self-consistent homogenization plasticity model proposed by Stringfellow and Parks [32,37] for alloys with strain-induced martensitic transformation, the macroscopic stress is described by the volume fraction, plastic strain, and rate-dependent mechanical properties of austenite and α' martensite. Bhattacharyya and Weng [47] proposed a constitutive model for metals with strain-induced martensitic phase transformation in which the effective flow stress is estimated based on the potential energy and change in the Gibbs free energy due to phase transformation, and the effective strain was taken to be the sum of plastic strain and transformation strain, computed using the lattice parameters of austenite and α' martensite.

Unlike micromechanics-based models, phenomenological models directly define the constitutive equations at the macroscopic scale. Miller and McDowell [50] proposed a

macroscopic plasticity model for fcc metals with strain-induced martensitic transformation, in which the effect of martensitic transformation on mechanical behavior was incorporated in the hardening function. Hänsel et al. [39] proposed a temperature-dependent plasticity model for TRansformation Induced Plasticity (TRIP) steels, which includes a von Mises yield surface and an isotropic hardening law, in which the flow stress is a function of α' martensite content, temperature, and plastic strain. Mohr and Jacquemin [40] developed a macroscopic plasticity model for anisotropic austenitic stainless steels, consisting of a Hill'48 yield surface [52], an associated flow rule, and a non-associated anisotropic hardening law to capture direction-dependent strain hardening. Beese and Mohr [41] proposed a stress state-dependent plasticity model for austenitic stainless steels, composed of a Hill'48 yield surface [52] with a nonlinear kinematic hardening law, an associated flow rule, and an isotropic hardening law coupled with a stress state-dependent strain-induced martensitic transformation kinetics equation to account for strain hardening due to phase transformation.

While plasticity models for texture-free conventionally processed austenitic stainless steels undergoing strain-induced martensitic transformation have been developed [25,32,39–41,43–50], thus far, no work has experimentally characterized or computationally predicted the multiaxial behavior of additively manufactured stainless steels, which may have preferred crystallographic texture. The objective of this work was to experimentally investigate, and propose a model for, the multiaxial plasticity behavior of additively manufactured SS304L. The proposed model consists of a von Mises yield surface, an associated flow rule, and an isotropic hardening law that is coupled with a stress state-, texture-, and chemistry-dependent, martensitic transformation kinetics equation proposed in a companion study by the authors [53]. The plasticity model was implemented into a finite element software, and calibrated using experimental data under

uniaxial tension, uniaxial compression, and pure shear, and validated through combined tension and shear experiments. This newly proposed model can be used to capture the microstructure-dependent constitutive behavior of textured metastable austenitic stainless steels.

2. Experimental methods

2.1. Materials

A previous study by the authors on additively manufactured SS304L showed that no martensitic transformation was observed in the as-built components deposited using pre-alloyed SS304L powder, as the powder was gas atomized in nitrogen, which stabilizes austenite [54]. Thus, to investigate the effect of powder chemistry on strain-induced martensitic transformation and mechanical behavior, two walls measuring 140 mm long, 104 mm tall, and 14 mm thick were built onto annealed 304L stainless steel substrates (ASTM A479 standard [55]) by DED AM from mixtures of pre-alloyed SS304L powder and pure iron powder. One wall was made using 90 vol.% pre-alloyed SS304L powder mixed with 10 vol.% iron powder, denoted as the 90% SS304L wall, and the other was made using 80 vol.% pre-alloyed SS304L powder mixed with 20 vol.% iron powder, denoted as the 80% SS304L wall. The pre-alloyed SS304L powder was gas atomized in nitrogen (Carpenter Powder Products, Corp.) and had the elemental composition given in Table 1. The iron powder was made by hydrogen reduction (Atlantic Equipment Engineers), and had a purity of 99.8%. The diameters of the both types of powder used ranged from 45 μm to 145 μm.

Both walls were fabricated using a custom-built DED AM system equipped with an ytterbium fiber laser (IPG Photonics® YLR-12000-L) operating at a wavelength of 1070 to 1080 nm. A laser power of 2 kW, scanning speed of 10.6 mm/s, and laser spot size of 4 mm in

diameter were used in deposition. Pre-mixed powder was fed at a powder flow rate of 15.5 g/min by four nozzles about 10 mm above the substrate. The hatch spacing was 2.5 mm and the layer thickness was 1.1 mm. These parameters were selected because previous components made using these processing parameters were found to be fully dense [54].

2.2. Uniaxial tension

Longitudinal and transverse uniaxial tension specimens, whose gauge regions measured 21.5 mm long, 4 mm wide, and 1.5 mm thick, complying with ASTM E8 [56], were extracted from the two as-built walls by wire electrical discharge machining (EDM). As discussed in previous studies by the authors, the mechanical properties varied in the vertical build direction due to two key factors. First, volatile elements selectively vaporized from the melt pool as the melt pool temperature increased with distance from the baseplate due to heat buildup during fabrication. Second, the austenite grain size increased with distance from the substrate, also due to heat buildup during fabrication that resulted in decreasing cooling rate with increasing distance from the substrate. These spatial variations in chemistry and grain size along the vertical direction of the builds resulted in location-dependent microstructural transformation, and therefore mechanical properties, in these walls [54,57]. In order to eliminate the effect of spatial variations in chemistry and grain size on the mechanical behavior, all of the mechanical test specimens in this study were extracted such that their gauge centers were located at the same height, about 40 mm above the bottom of each wall. The residual stresses present in the as-built wall were assumed to be relieved in the relatively small extracted test specimens [53]. The chemical compositions of this location in both walls are given in Table 1.

Uniaxial tension tests were performed on an electromechanical test frame (Instron 4202, 10 kN load cell) at a strain rate of 1.2×10^{-3} /s. The deformation fields of the gauge region were

measured using Digital Image Correlation (DIC). For DIC, each sample was painted white with a black speckle pattern on top. The images of the deformed gauge region were captured by a digital camera (Point Grey GRAS-50S5M-C) at 1 Hz during deformation. The surface deformation fields were calculated by applying a cubic B-spline interpolation algorithm in the correlation software (Vic2D, Correlated Solutions). During the analysis, a subset of 21 pixels and a step size of 5 pixels were used, resulting in a virtual strain gauge size of 56 pixels or 1.5 mm [58]. The axial strain was measured using a 21 mm-long vertical virtual extensometer. The evolution of the volume fraction of α' martensite was measured through magnetic permeability measurements using a feritescope (Fisher Feritescope FMP 30), as described in the companion study by the authors [53].

2.3. Uniaxial compression

Longitudinal and transverse cylindrical compression specimens measuring 16 mm in length and 8 mm in diameter were extracted by wire EDM from the two as-built walls. Uniaxial compression tests were performed at a strain rate of 1.5×10^{-5}/s on a hydraulic test frame (MTS Systems Corp.). The evolution of α' martensite was characterized by *in situ* neutron diffraction using the VULCAN instrument at the Spallation Neutron Source at Oak Ridge National Laboratory [59–61]. The details of neutron diffraction results can be found in the companion study [53].

2.4. Multiaxial loading

Longitudinal plasticity specimens, with dimensions shown in Figure 1, were also extracted from the two as-built walls by wire EDM for a 1.5 mm thick 2D contour, with milling used for the reduced thickness gauge section. The width-to-height ratio of 10 and thin gauge region

results in plane strain along the transverse (T), or vertical build, direction and plane stress through the thickness (z direction) in these specimens [62].

Multiaxial loading tests were performed using a custom-built dual actuator hydraulic test frame (MTS Systems Corp.). The test frame is equipped with two 100 kN load cells to measure the vertical force and one 50 kN load cell to measure the horizontal force. The ratio of the applied vertical force to applied horizontal force, $\frac{F_v}{F_h}$, is described by a biaxial loading angle, β, as:

$$tan\beta = \frac{F_v}{F_h} \quad (1)$$

such that $\beta = 0^o$ corresponds to pure shear, $\beta = 90^o$ corresponds to plane strain tension, and $0^o < \beta < 90^o$ corresponds to combined tension and shear. In this study, β values of 0^o, 30^o, and 60^o were examined and the loading conditions for all the tests are given in Table 2.

DIC was used to analyze the strain fields of the gauge center with a subset of 25 pixels and a step size of 6 pixels, corresponding to a virtual strain gauge size of 67 pixels or 0.8 mm [58]. To compute vertical and horizontal strains, 3 mm-long vertical and horizontal virtual extensometers were used. The evolution of α' martensite content with respect to plastic strain was measured using a feritescope, as described in [53].

3. Plasticity model

A macroscopic constitutive model was developed to describe the multiaxial plasticity behavior of additively manufactured SS304L with preferred crystallographic texture under quasi-static loading at room temperature. The proposed model includes a yield surface, an associated flow rule, and an isotropic hardening law. The hardening law incorporates the effect of martensite content on multiaxial plasticity behavior through the coupling of the microstructural

transformation kinetics equation to the hardening law. The hardening law also incorporates typical, dislocation-driven, strain hardening. The model was implemented into the commercial finite element software (ABAQUS/Explicit 6.14 [63]), calibrated, and validated.

3.1. Yield surface

The yield surface is defined by:

$$f = \bar{\sigma} - k = 0 \tag{2}$$

where $\bar{\sigma}$ is the equivalent stress and k is the deformation resistance or flow stress.

Previous studies by the authors [54,57] showed that there was no notable anisotropy in the yield strength of the additively manufactured SS304L. Therefore, the isotropic von Mises yield criterion was adopted, and Eqn. (2) becomes:

$$\bar{\sigma}_{vM} - k = 0 \tag{3}$$

where $\bar{\sigma}_{vM}$ is the von Mises equivalent stress, described as:

$$\bar{\sigma}_{vM} = \sqrt{3J_2} = \sqrt{\frac{3}{2}\underline{\underline{\boldsymbol{s}}} \cdot \underline{\underline{\boldsymbol{s}}}} \tag{4}$$

where J_2 is the second invariant of the deviatoric stress tensor, $\underline{\underline{\boldsymbol{s}}}$.

In the plane stress condition, the normal and shear stress components in the z direction are negligible, and therefore, approximated as zero. Thus, the stress tensor, $\underline{\underline{\boldsymbol{\sigma}}}$, can be expressed by a stress vector, $\underline{\boldsymbol{\sigma}}$, as:

$$\underline{\boldsymbol{\sigma}} = \{\sigma_L, \sigma_T, \tau\}^T \tag{5}$$

where σ_L and σ_T are normal stresses along the longitudinal (L) and transverse (T) directions, as shown in Figure 1, and τ is the in-plane shear stress.

Under plane stress, the von Mises yield equivalent stress becomes:

$$\bar{\sigma}_{vM} = \sqrt{{\sigma_L}^2 - \sigma_L\sigma_T + {\sigma_T}^2 + 3\tau} \tag{6}$$

3.2. Associated flow rule

An associated flow rule is used to describe the evolution of plastic strain with applied stress, which is given as:

$$\mathrm{d}\underline{\underline{\boldsymbol{\varepsilon}}}^{P} = d\lambda \frac{\partial \bar{\sigma}_{vM}}{\partial \underline{\underline{\boldsymbol{\sigma}}}} \tag{7}$$

where $\mathrm{d}\underline{\underline{\boldsymbol{\varepsilon}}}^{P}$ is the increment of plastic strain, and $d\lambda$ is the plastic multiplier.

3.3. Isotropic hardening law

In SS304L, the strain hardening is due to both dislocation interactions and the increase in volume fraction of the stronger martensite phase during plastic deformation due to the isotropic strain-induced martensitic phase transformation [53]. To account for the contribution from both of these effects, an isotropic hardening law is adopted from [41] to describe the evolution of deformation resistance, *k*, with plastic deformation, and given as:

$$dk = H_{\varepsilon} d\bar{\varepsilon}_{vM}^{P} + H_{c} dc \tag{8}$$

where H_{ε} and H_c are hardening moduli, $d\bar{\varepsilon}_{vM}^{P}$ is the increment of von Mises equivalent plastic strain, and *dc* is the increment of α' martensite volume fraction.

The first term in Eqn. (8) describes the strain hardening from dislocation pileup during plastic deformation and is assumed to follow a Swift hardening law [64], as:

$$k = A(\varepsilon_0 + \bar{\varepsilon}_{vM}^{P})^{m} + k_0 \tag{9}$$

where *A* is the stress amplitude, ε_0 is the strain shift parameter, *m* is the hardening exponent, and k_0 is the stress shift parameter. As a result, the hardening modulus, H_{ε}, is expressed as:

$$H_{\varepsilon} = \frac{dk}{d\bar{\varepsilon}_{vM}^{P}} = Am(\varepsilon_0 + \bar{\varepsilon}_{vM}^{P})^{m-1} \tag{10}$$

As Eqns. (9) and (10) describe the strain hardening only due to dislocation interactions, *A*, ε_0, *m*, and k_0 are assumed to be the same for the two walls with different chemistries.

The second term in Eqn. (8) describes the strain hardening due to the increase of α' martensite content. As the influence of chemistry on strain-induced martensitic transformation is captured by d*c*, which is described in Section 3.4, the hardening modulus, H_c, is assumed to be chemistry independent.

3.4. Strain-induced martensitic transformation kinetics

The stress state-, texture- and chemistry-dependent strain-induced martensitic transformation kinetics equation developed in the companion study [53] is adopted here to describe the α' martensite volume fraction as a function of plastic strain. The stress state may be defined by two parameters: the stress triaxiality and Lode angle parameter [33,65]. The stress triaxiality, η, is defined as:

$$\eta = \frac{\sigma_m}{\bar{\sigma}_{vM}} \tag{11}$$

where σ_m is the hydrostatic stress, which is proportional to the first invariant, I_1, of the stress tensor, which is $\sigma_m = \frac{1}{3} I_1 = \frac{1}{3} tr(\underline{\boldsymbol{\sigma}})$.

The Lode angle parameter, $\bar{\theta}$, is a function of the second and third invariants of the deviatoric stress tensor, J_2 and J_3, and is expressed as:

$$\bar{\theta} = 1 - \frac{2}{\pi} arccos\left(\frac{3\sqrt{3}}{2}\frac{J_3}{\sqrt{{J_2}^3}}\right) \text{ and } J_3 = det\left(\underline{\boldsymbol{s}}\right). \tag{12}$$

The values of stress triaxiality and Lode angle parameter of the stress states studied are given in Table 3. The effect of texture on strain-induced martensitic transformation is captured by the driving force for austenite-to-α' martensite transformation, *W*, which depends on texture and applied stress state [53].

The differential form of the strain-induced martensitic transformation kinetics equation adopted from [53] is given as:

$$dc = (c_{max} - c)nD(D\bar{\varepsilon}_{vM}^{P})^{n-1}d\bar{\varepsilon}_{vM}^{P} \quad (13)$$

where c_{max} is the saturation value of the volume fraction of strain-induced α' martensite, and *n* and *D* are material parameters. Here, we assume that the parameter *D* may be taken to be a function of η, $\bar{\theta}$, and *W*, as:

$$D = D_0 + a_\eta \eta + a_{\theta 1}\bar{\theta} + a_{\theta 2}\bar{\theta}^2 + a_W W \quad (14)$$

where D_0, a_η, $a_{\theta 1}$, $a_{\theta 2}$, and a_W are material parameters, in which a_η, $a_{\theta 1}$, $a_{\theta 2}$, and a_W describe the effect of η, $\bar{\theta}$, and *W* on the rate of phase transformation [53]. Among all the parameters in Eqns. (13) and (14), c_{max} and *n* are taken to be chemistry dependent, D_0, a_η, a_θ, and a_W are material constants, and *D* is taken to be stress state- and texture-dependent.

4. Results and discussion

4.1. Overview

As described in the companion study [53], the as-built SS304L walls studied herein consisted of elongated austenite grains along the vertical build direction. This resulted in a predominant crystallographic texture of {111} <1$\bar{1}$0> in these walls, in which <111> was parallel to the longitudinal direction and <1$\bar{1}$0> was parallel to the transverse direction of the walls.

Representative stress-strain curves for longitudinal specimens from the two walls are given in Figure 2. Within the same wall, the strain hardening rate, defined as the slope of the stress-strain curve, was highest under uniaxial compression, followed by uniaxial tension, and lowest under pure shear, which can be explained by the stress state-dependent martensitic transformation kinetics. As shown in this study's companion paper [53], the rate of strain-induced martensitic transformation with respect to plastic strain from high to low was uniaxial compression, uniaxial

tension, and pure shear, which is consistent with the trend in strain hardening rate with respect to stress state seen here.

Under the same stress state, and for any given plastic strain, the 80% SS304L wall had a higher flow stress than the 90% SS304L wall. With increasing iron, the relative content of elements that increase the stacking fault energy in austenite, and therefore impede austenite-to-α' martensite phase transformation (silicon, manganese, chromium, and nickel), decreased. This decrease in stacking fault energy with the decrease in the relative concentration of alloying elements resulted in the increase in the rate of strain-induced martensitic transformation with respect to plastic strain [57]. Therefore, the 80% SS304L wall had a higher martensitic transformation rate and flow stress at a given plastic strain, compared to the 90% SS304L wall.

4.2. Model calibration

The experimentally measured 0.2% offset yield strengths under different stress states, for both walls, are plotted on the von Mises yield surface, as shown in Figure 3. As all the points lie on or close to the yield surface, the von Mises yield criterion is sufficient to describe the yield surfaces for the walls studied. Note that the textured microstructures in the two walls did not result in anisotropic yield strength, which may be partially due to the notable variability in properties of samples along the same orientation.

The plasticity model was implemented into a commercial finite element code (ABAQUS/Explicit 6.14 [63]). A shell element (type S4R) with a side length of 1 mm and a thickness of 1.5 mm was used to represent the gauge center of each specimen. The strain-induced martensitic transformation kinetics equation parameters (c_{max}, n, D_0, a_η, $a_{\theta 1}$, $a_{\theta 2}$, and a_W) were calibrated for the 80% and 90% SS304L walls in the companion study [53]. The remaining model parameters that required identification in this study were the strain hardening

parameters (A, ε_0, m, k_0, and H_c). These parameters were first estimated using experimentally measured true stress-strain curves from uniaxial tension, and a range defined as 0.5 x estimated value to 1.5 x estimated value was assigned to each parameter. To calibrate the model parameters, the stress-strain behavior under three stress states (uniaxial tension, uniaxial compression, and shear), and for each of the walls, was computed using over 1000 simulations with different combinations of the varying model inputs. For each simulation, a set of parameters s_i = {A, ε_0, m, k_0, and H_c}, each within their prescribed range, was randomly selected based on the assumption of a uniform value distribution within each range. Using these parameters, the stress, $\sigma_{sim,j}(s_i)$, was computed for a given experimentally studied strain history, where j is the number of stress states used for model calibration. A cost function was evaluated for each set of parameters, defined as:

$$\chi(s_i) = \sum_{j=1}^{J} \left| \frac{\sigma_{sim,j}(s_i) - \sigma_{exp,j}}{\sigma_{exp,j}} \right| \quad (15)$$

where $\sigma_{exp,j}$ is the experimentally measured engineering stress. The optimized set of model parameters was chosen as that which minimized χ.

In the present study, experimental stress-strain curves of longitudinal specimens from uniaxial tension, uniaxial compression, and pure shear from the two walls were used for model calibration, giving J = 6. Lack-of-fusion pores along the laser scanning direction, or perpendicular to the vertical build direction, were observed in the two walls. When tension is applied along the build direction, the presence of these pores reduces the ductility of the sample, thus limiting the amount of plastic strain achieved, and therefore, the amount of strain-induced martensite that develops [57]. Therefore, only data from longitudinal specimens were used for model calibration and validation. The calibrated model parameters are given in Table 4.

4.3. Comparison between simulation and experimental results

The experimentally measured engineering stress–strain curves under uniaxial tension, uniaxial compression, and pure shear from the two walls are plotted in Figure 4 together with those produced by the calibrated model. Table 5 summarizes the maximum stress difference between simulation and experimental results for each stress state. As shown in Table 5, among all the stress states, the simulations have a maximum difference in flow stress of 5% from the experimental stress level in the 80% SS304L wall and 4% in the 90% SS304L wall. The good agreement between the computationally modeled and experimentally measured results indicates that the plasticity model coupled with the underlying phase transformation equation is able to capture the multiaxial plasticity behavior of additively manufactured SS304L.

4.4. Model validation

In order to validate the plasticity model, simulations of combined tension/shear loading with $\beta = 30^{o}$ and 60^{o} were performed and compared to the experimentally measured data for these same two loading conditions. The finite element simulations were also conducted using a shell element (S4R) with a side length of 1 mm and a thickness of 1.5 mm. The predicted engineering stress-strain curves are in good agreement with experimentally measured curves, as shown in Figure 4. The maximum stress difference between simulation predictions and experimental results is also given in Table 5, which shows the difference between the simulation and experimental results is within 7% from the experimental stress level in the 80% SS304L wall and 9% in the 90% SS304L wall under combined loading. The small difference between computationally predicted and experimentally measured curves indicates that the proposed plasticity model is able to predict the mechanical behavior of additively manufactured SS304L under multiaxial stress states.

While some existing plasticity models can presumably be calibrated to capture the mechanical behavior of texture-free austenitic stainless steels [25,32,39–50], these do not couple the stress-state microstructural evolution with crystallographic texture. In additively manufactured austenitic stainless steels, texture is observed due to the columnar grain growth along the vertical build direction. The newly proposed plasticity model provides insights into experiments needed to measure, and a modeling approach to capture and predict, the multiaxial plasticity behavior of textured austenitic stainless steels.

5. Summary and conclusions

Two walls, with chemical compositions varying from the AISI SS304L prescribed composition, were fabricated by DED AM and subjected to a range of stress states to investigate the multiaxial plasticity behavior of these materials. This understanding of multiaxial behavior is imperative for the adoption of AM, for which complex shaped components under load will be subjected to a range of stress states. Based on the experimental observations, a macroscopic plasticity model is proposed for the materials. The primary findings of this study are as follows:

- The plasticity behavior of additively manufactured SS304L walls depends on stress state and chemistry. In a single wall subjected to multiaxial stress states, the strain hardening rate (with respect to plastic strain) was highest in uniaxial compression, lowest in pure shear, and intermediate in uniaxial tension. In the two walls under the same stress state, the wall with lower stacking fault energy, and therefore, lower austenite stability due to higher iron content, had a higher rate of strain-induced martensitic transformation and flow stress at a given plastic strain.

- A plasticity model consisting of a von Mises yield surface, an associated flow rule, and an isotropic hardening law coupled with a stress state-, texture-, and chemistry-dependent strain-induced martensitic transformation kinetics equation is able to capture and predict the constitutive behavior of additively manufactured SS304L under multiaxial stress states. This is due to the fact that the hardening equation takes into consideration the combined effects of strain hardening from dislocation mechanisms and the strain hardening due to the microstructural phase transformation, or the increase in the volume fraction of the harder martensite phase with plastic deformation.
- The plasticity model proposed provides a framework for describing and predicting the constitutive behavior of texture-free and textured metastable austenitic stainless steels in structural applications under multiaxial stress states, and in particular, linking the macroscopic deformation behavior to the physical strengthening mechanisms at the microscale.

Acknowledgments

The authors gratefully acknowledge the financial support provided by the National Science Foundation through award number CMMI-1402978 and CMMI-1652575. Any opinions, findings, and conclusions or recommendations in the materials are those of the authors and do not necessarily reflect the views of the Nation Science Foundation. Samples were fabricated at Penn State's Center for Innovation Materials Processing through Direct Digital Deposition (CIMP-3D). We acknowledge Dr. Dong Ma of ORNL for performing uniaxial compression tests.

Data Availability

All relevant data are available from the authors.

References

[1] D.D. Gu, W. Meiners, K. Wissenbach, R. Poprawe, Laser additive manufacturing of metallic components: materials, processes and mechanisms, Int. Mater. Rev. 57 (2012) 133–164. doi:10.1179/1743280411Y.0000000014.

[2] X. Wu, A review of laser fabrication of metallic engineering components and of materials, Mater. Sci. Technol. 23 (2007) 631–640. doi:10.1179/174328407X179593.

[3] ASTM F2792: Standard Terminology for Additive Manufacturing Technologies, in: ASTM Stand., West Conshohocken, PA, 2012: pp. 1–3. doi:10.1520/F2792-12A.2.

[4] A.M. Beese, B.E. Carroll, Review of Mechanical Properties of Ti-6Al-4V Made by Laser-Based Additive Manufacturing Using Powder Feedstock, JOM. 68 (2016) 724–734. doi:10.1007/s11837-015-1759-z.

[5] Z. Wang, A.D. Stoica, D. Ma, A.M. Beese, Stress relaxation in a nickel-base superalloy at elevated temperatures via in situ neutron diffraction characterization: application to additive manufacturing, Mater. Sci. Eng. A. 714 (2018) 75–83. doi:10.1016/j.msea.2017.09.071.

[6] Z. Wang, A.D. Stoica, D. Ma, A.M. Beese, Stress relaxation behavior and mechanisms in Ti-6Al-4V determined via in situ neutron diffraction: Application to additive manufacturing, Mater. Sci. Eng. A. 707 (2017) 585–592. doi:https://doi.org/10.1016/j.msea.2017.09.071.

[7] W.E. Frazier, Metal additive manufacturing: A review, J. Mater. Eng. Perform. 23 (2014) 1917–1928. doi:10.1007/s11665-014-0958-z.

[8] H.K. Rafi, D. Pal, N. Patil, T.L. Starr, B.E. Stucker, Microstructure and Mechanical

Behavior of 17-4 Precipitation Hardenable Steel Processed by Selective Laser Melting, J. Mater. Eng. Perform. 23 (2014) 4421–4428. doi:10.1007/s11665-014-1226-y.

[9] Z. Wang, K. Guan, M. Gao, X. Li, X. Chen, X. Zeng, The microstructure and mechanical properties of deposited-IN718 by selective laser melting, J. Alloys Compd. 513 (2012) 518–523. doi:10.1016/j.jallcom.2011.10.107.

[10] D.W. Brown, D.P. Adams, L. Balogh, J.S. Carpenter, B. Clausen, G. King, B. Reedlunn, T.A. Palmer, M.C. Maguire, S.C. Vogel, In Situ Neutron Diffraction Study of the Influence of Microstructure on the Mechanical Response of Additively Manufactured 304L Stainless Steel, Metall. Mater. Trans. A. (2017) 1–15. doi:10.1007/s11661-017-4330-4.

[11] A.M. Beese, Z. Wang, A.D. Stoica, D. Ma, Absence of dynamic strain aging in an additively manufactured nickel-base superalloy, Nat. Commun. 9 (2018) 2083.

[12] W. Gao, Y. Zhang, D. Ramanujan, K. Ramani, Y. Chen, C.B. Williams, C.C.L. Wang, Y.C. Shin, S. Zhang, P.D. Zavattieri, The status, challenges, and future of additive manufacturing in engineering, Comput. Des. (2015). doi:10.1016/j.cad.2015.04.001.

[13] T. DebRoy, H.L. Wei, J.S. Zuback, T. Mukherjee, J.W. Elmer, J.O. Milewski, A.M. Beese, A. Wilson-Heid, A. De, W. Zhang, Additive manufacturing of metallic components – Process, structure and properties, Prog. Mater. Sci. 92 (2018) 112–224. doi:10.1016/j.pmatsci.2017.10.001.

[14] K. Zhang, S. Wang, W. Liu, X. Shang, Characterization of stainless steel parts by Laser Metal Deposition Shaping, Mater. Des. 55 (2014) 104–119. doi:10.1016/j.matdes.2013.09.006.

[15] M.S.F. de Lima, S. Sankaré, Microstructure and mechanical behavior of laser additive

manufactured AISI 316 stainless steel stringers, Mater. Des. 55 (2014) 526–532. http://linkinghub.elsevier.com/retrieve/pii/S0261306913009436 (accessed August 29, 2014).

[16] A.E. Wilson-Heid, Z. Wang, B. McCornac, A.M. Beese, Quantitative relationship between anisotropic strain to failure and grain morphology in additively manufactured Ti-6Al-4V, Mater. Sci. Eng. A. 706 (2017) 287–294. doi:10.1016/j.msea.2017.09.017.

[17] B.E. Carroll, T.A. Palmer, A.M. Beese, Anisotropic tensile behavior of Ti–6Al–4V components fabricated with directed energy deposition additive manufacturing, Acta Mater. 87 (2015) 309–320. doi:10.1016/j.actamat.2014.12.054.

[18] B. AlMangour, J.M. Yang, Understanding the deformation behavior of 17-4 precipitate hardenable stainless steel produced by direct metal laser sintering using micropillar compression and TEM, Int. J. Adv. Manuf. Technol. 90 (2017) 119–126. doi:10.1007/s00170-016-9367-9.

[19] I. Tolosa, F. Garciandía, F. Zubiri, F. Zapirain, A. Esnaola, Study of mechanical properties of AISI 316 stainless steel processed by "selective laser melting", following different manufacturing strategies, Int. J. Adv. Manuf. Technol. 51 (2010) 639–647. doi:10.1007/s00170-010-2631-5.

[20] M. Rombouts, G. Maes, M. Mertens, W. Hendrix, Laser metal deposition of Inconel 625: Microstructure and mechanical properties, J. Laser Appl. 24 (2012) 1–6. doi:10.2351/1.4757717.

[21] M.L. Griffith, D.M. Keicher, C.L. Atwood, J.A. Romero, E. Smugeresky, L.D. Harwell, D.L. Greene, J.E. Smugeresky, L.D. Harwell, D.L. Greene, Free Form Fabrication of Metallic Components Using Laser Engineered Net Shaping (LENS^{TM}), in: 7th Solid Free.

Fabr. Symp., Austin, TX, 1996: pp. 125–132. doi:10.4028/www.scientific.net/AMR.15-17.175.

[22] M.L. Griffith, M.T. Ensz, J.D. Puskar, C. V. Robino, J.A. Brooks, J.A. Philliber, E. Smugeresky, J.E. Smugeresky, W.H. Hofmeister, Understanding the Microstructure and Properties of Components Fabricated by Laser Engineered Net Shaping (LENS), in: Mater. Res. Soc. Symp., 2000: pp. 9–20. doi:10.1557/PROC-625-9.

[23] J. Yu, M. Rombouts, G. Maes, Cracking behavior and mechanical properties of austenitic stainless steel parts produced by laser metal deposition, Mater. Des. 45 (2013) 228–235. doi:10.1016/j.matdes.2012.08.078.

[24] M. Ma, Z. Wang, D. Wang, X. Zeng, Control of shape and performance for direct laser fabrication of precision large-scale metal parts with 316L Stainless Steel, Opt. Laser Technol. 45 (2013) 209–216. doi:10.1016/j.optlastec.2012.07.002.

[25] Lecroise.F, A. Pineau, Martensitic Transformations Induced By Plastic-Deformation in Fe-Ni-Cr-C System, Metall. Trans. 3 (1972) 387–396.

[26] J.R. Patel, M. Cohen, Criterion for the action of applied stress in the martensitic transformation, Acta Metall. 1 (1953) 531–538. doi:10.1016/0001-6160(53)90083-2.

[27] D. Mohr, M. Dunand, K.H. Kim, Evaluation of associated and non-associated quadratic plasticity models for advanced high strength steel sheets under multi-axial loading, Int. J. Plast. 26 (2010) 939–956. doi:10.1016/j.ijplas.2009.11.006.

[28] M. Coret, S. Calloch, A. Combescure, Experimental study of the phase transformation plasticity of 16MND5 low carbon steel under multiaxial loading, Int. J. Plast. 18 (2002) 1707–1727.

[29] T. Angel, Formation of Martensite in Austenitic Stainless Steels, effect of deformation,

temperature and composition, J. Iron Steel Inst. (1954) 165–174.

[30] G.B. Olson, M. Cohen, Kinetics of strain-induced martensitic nucleation, Metall. Trans. A. 6 (1975) 791–795. doi:10.1007/BF02672301.

[31] J.B. Leblond, Mathematical modelling of transformation plasticity in steels II: Coupling with strain hardening phenomena, Int. J. Plast. 5 (1989) 573–591. doi:10.1016/0749-6419(89)90002-8.

[32] R.G. Stringfellow, D.M. Parks, A self-consistent model of isotropic viscoplastic behavior in multiphase materials, Int. J. Plast. 7 (1991) 529–547.

[33] A.M. Beese, D. Mohr, Effect of stress triaxiality and Lode angle on the kinetics of strain-induced austenite-to-martensite transformation, Acta Mater. 59 (2011) 2589–2600. http://linkinghub.elsevier.com/retrieve/pii/S1359645410008724.

[34] B.L. Ennis, E. Jimenez-Melero, E.H. Atzema, M. Krugla, M.A. Azeem, D. Rowley, D. Daisenberger, D.N. Hanlon, P.D. Lee, Metastable austenite driven work-hardening behaviour in a TRIP-assisted dual phase steel, Int. J. Plast. 88 (2017) 126–139. doi:10.1016/j.ijplas.2016.10.005.

[35] Y. Li, W. Li, J.C. Hu, H.M. Song, X.J. Jin, Compatible strain evolution in two phases due to epsilon martensite transformation in duplex TRIP-assisted stainless steels with high hydrogen embrittlement resistance, Int. J. Plast. 88 (2017) 53–69. doi:10.1016/j.ijplas.2016.09.012.

[36] F.D. Fischer, G. Reisner, E. Werner, K. Tanaka, G. Cailletaud, T. Antretter, New view on transformation induced plasticity (TRIP), Int. J. Plast. 16 (2000) 723–748. doi:10.1016/S0749-6419(99)00078-9.

[37] R.G. Stringfellow, D.M. Parks, G.B. Olson, A constitutive model for transformation

plasticity accompanying strain-induced martensitic transformations in metastable austenitic steels, Acta Metall. Mater. 40 (1992) 1703–1716. doi:10.1016/0956-7151(92)90114-T.

[38] A. Creuziger, T. Foecke, Transformation potential predictions for the stress-induced austenite to martensite transformation in steel, Acta Mater. 58 (2010) 85–91. doi:10.1016/j.actamat.2009.08.059.

[39] A.H.C. Hänsel, P. Hora, J. Reissner, Model for the kinetics of strain-induced martensitic phase transformation at non-isothermal conditions for the simulation of sheet metal forming processes with metastable austenitic steels, in: J. Huétink, F.P.T. Baaijens (Eds.), Simul. Mater. Process. Theory, Methods, Appl., Balkema, Rotterdam, 1998: pp. 373–378.

[40] D. Mohr, J. Jacquemin, Large deformation of anisotropic austenitic stainless steel sheets at room temperature: Multi-axial experiments and phenomenological modeling, J. Mech. Phys. Solids. 56 (2008) 2935–2956. doi:10.1016/j.jmps.2008.07.003.

[41] A.M. Beese, D. Mohr, Anisotropic plasticity model coupled with Lode angle dependent strain-induced transformation kinetics law, J. Mech. Phys. Solids. 60 (2012) 1922–1940. doi:10.1016/j.jmps.2012.06.009.

[42] L. Taleb, F. Sidoroff, A micromechanical modeling of the Greenwood-Johnson mechanism in transformation induced plasticity, Int. J. Plast. 19 (2003) 1821–1842. doi:10.1016/S0749-6419(03)00020-2.

[43] P.-O. Santacreu, J.-C. Glez, G. Chinouilh, T. Frohlich, Behaviour model of austenitic stainless steels for automotive structural parts, Steel Res. Int. 77 (2006) 686–691.

[44] H. Hallberg, P. Håkansson, M. Ristinmaa, A constitutive model for the formation of martensite in austenitic steels under large strain plasticity, Int. J. Plast. 23 (2007) 1213–

1239. doi:10.1016/j.ijplas.2006.11.002.

[45] J. Post, K. Datta, J. Beyer, A macroscopic constitutive model for a metastable austenitic stainless steel, Mater. Sci. Eng. A. 485 (2008) 290–298. doi:10.1016/j.msea.2007.07.084.

[46] J.B. Leblond, G. Mottet, J.C. Devaux, A theoretical and numerical approach to the plastic behaviour of steels during phase transformations-II. Study of classical plasticity for ideal-plastic phases, J. Mech. Phys. Solids. 34 (1986) 411–432. doi:10.1016/0022-5096(86)90010-4.

[47] A. Bhattacharyya, G.J. Weng, An energy criterion for the stress-induced martensitic transformation in a ductile system, J. Mech. Phys. Solids. 42 (1994) 1699–1724. doi:10.1016/0022-5096(94)90068-X.

[48] I. Papatriantafillou, N. Aravas, G.N. Haidemenopoulos, Finite element modelling of TRIP steels, Steel Res. Int. 75 (2004) 730–736.

[49] I. Papatriantafillou, M. Agoras, N. Aravas, G. Haidemenopoulos, Constitutive modeling and finite element methods for TRIP steels, Comput. Methods Appl. Mech. Eng. 195 (2006) 5094–5114. doi:10.1016/j.cma.2005.09.026.

[50] M.P. Miller, D.L. McDowell, Modeling large strain multiaxial effects in FCC polycrystals, Int. J. Plast. 12 (1996) 875–902. doi:10.1016/S0749-6419(96)00032-0.

[51] M. Cherkaoui, M. Berveiller, X. Lemoine, Couplings between plasticity and martensitic phase transformation: overall behavior of polycrystalline TRIP steels, Int. J. Plast. 16 (2000) 1215–1241. doi:10.1016/S0749-6419(00)00008-5.

[52] R. Hill, A theory of the yielding and plastic flow of anisotropic metals, Proc. R. Soc. Lond. A. Math. Phys. Sci. 193 (1948) 281–297.

[53] Z. Wang, A.M. Beese, Effect of stress state and texture on martensitic phase

transformation kinetics of additively manufactured austenitic stainless steel, Submitt. Publ. under Revis. (2018).

[54] Z. Wang, T.A. Palmer, A.M. Beese, Effect of processing parameters on microstructure and tensile properties of austenitic stainless steel 304L made by directed energy deposition additive manufacturing, Acta Mater. 110 (2016) 226–235. doi:10.1016/j.actamat.2016.03.019.

[55] ASTM A479/A479M: Standard Specification for Stainless Steel Bars and Shapes for Use in Boilers and Other Pressure Vessels, in: ASTM Int., West Conshohocken, PA, 2015: pp. 1–8. doi:10.1520/A0479.

[56] ASTM, ASTM Standard E8/E8M-16a: Standard Test Methods for Tension Test of Metallic Materials, in: ASTM Int., West Conshohocken, PA, 2016. doi:10.1520/E0008_E0008M-16A.

[57] Z. Wang, A.M. Beese, Effect of chemistry on martensitic phase transformation kinetics and resulting properties of additively manufactured stainless steel, Acta Mater. 131 (2017) 410–422.

[58] P. Reu, Virtual Strain Gage Size Study, Exp. Tech. 39 (2015) 1–3.

[59] K. An, H.D. Skorpenske, A.D. Stoica, D. Ma, X.L. Wang, E. Cakmak, First in situ lattice strains measurements under load at VULCAN, Metall. Mater. Trans. A Phys. Metall. Mater. Sci. 42 (2011) 95–99. doi:10.1007/s11661-010-0495-9.

[60] T. Ungar, A.D. Stoica, G. Tichy, X.-L. Wang, Orientation-dependent evolution of the dislocation density in grain populations with different crystallographic orientations relative to the tensile axis in a polycrystalline aggregate of stainless steel, Acta Mater. 66 (2014) 251–261. doi:10.1016/j.actamat.2013.11.012.

[61] G.M. Stoica, A.D. Stoica, M.K. Miller, D. Ma, Temperature-dependent elastic anisotropy and mesoscale deformation in a nanostructured ferritic alloy., Nat. Commun. 5 (2014) 1–8. doi:10.1038/ncomms6178.

[62] D. Mohr, M. Oswald, A new experimental technique for the multi-axial testing of advanced high strength steel sheets, Exp. Mech. 48 (2008) 65–77. doi:10.1007/s11340-007-9053-9.

[63] ABAQUS, Version 6.14 User's Manual, 2014.

[64] H.W. Swift, Plastic instability under plane stress, J. Mech. Phys. Solids. 1 (1952) 1–18. doi:10.1016/0022-5096(52)90002-1.

[65] Y. Bai, T. Wierzbicki, A new model of metal plasticity and fracture with pressure and Lode dependence, Int. J. Plast. 24 (2008) 1071–1096. doi:10.1016/j.ijplas.2007.09.004.

Figures

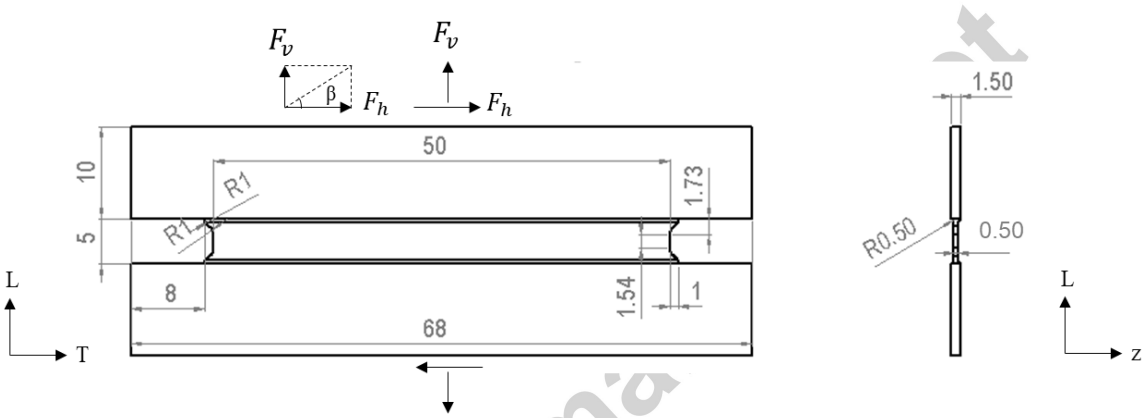

Figure 1. Geometry of a multiaxial plasticity specimen (units: mm), with the orientations of the vertical force, F_v, and horizontal force, F_h, along with the biaxial loading angle, β, drawn. Sample geometry adapted from [62]. L is the longitudinal direction, parallel to the length of the wall, T is the vertical build direction, and z is the wall thickness direction.

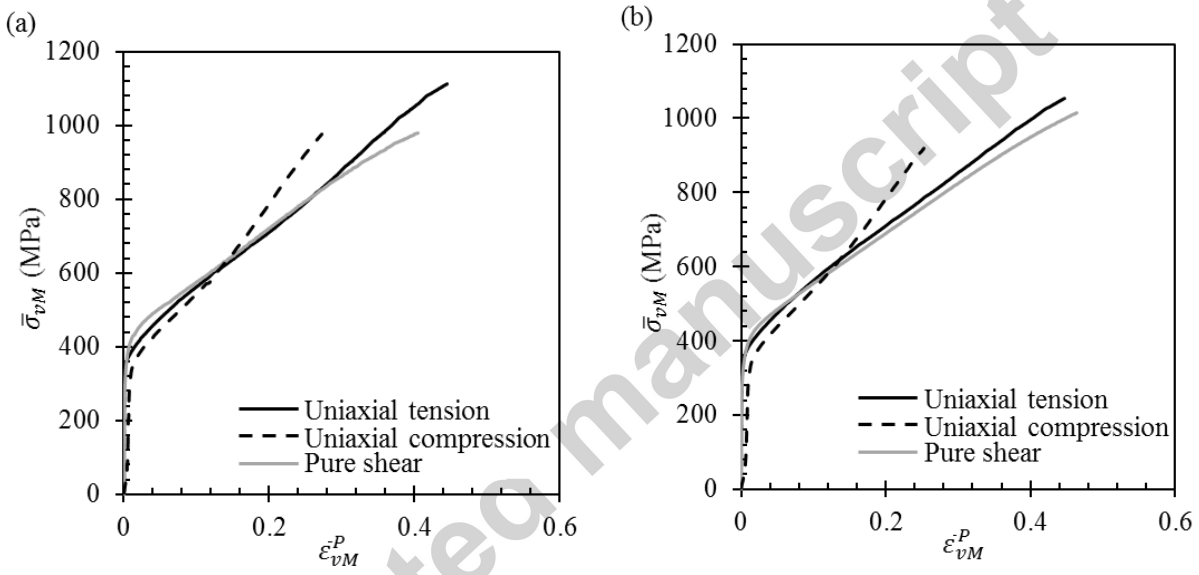

Figure 2. Von Mises equivalent stress, $\bar{\sigma}_{vM}$, versus von Mises equivalent plastic strain, $\bar{\varepsilon}^P_{vM}$, for representative tests on samples extracted from the (a) 80% SS304L wall, and (b) 90% SS304L wall.

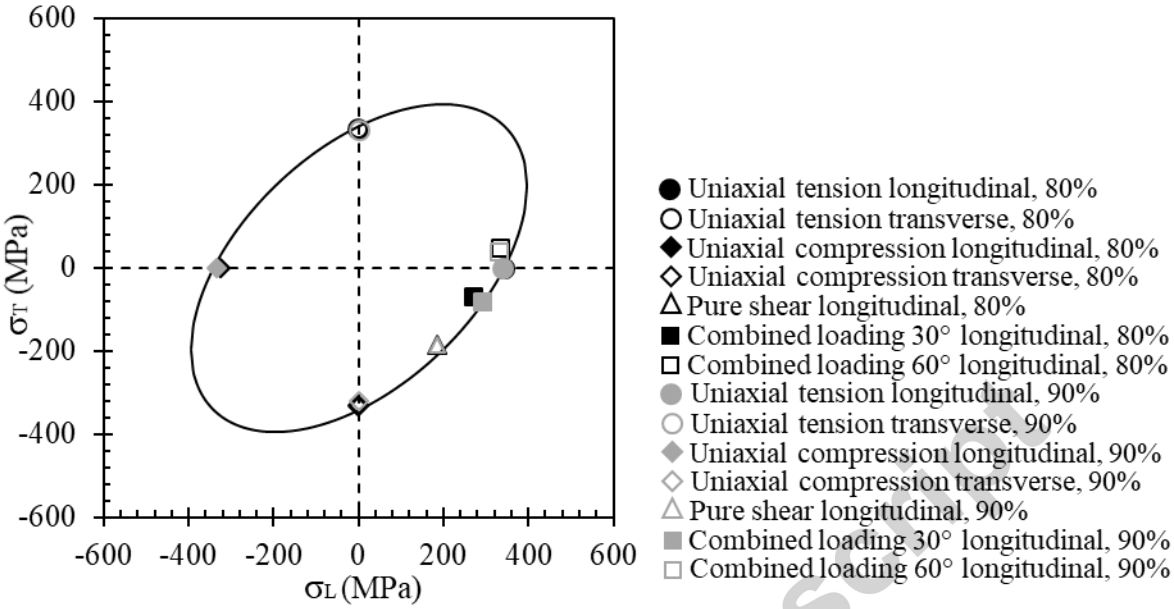

Figure 3. Engineering yield stress in the transverse direction, σ_T, versus engineering yield stress in the longitudinal direction, σ_L, for plane stress, in the 80% and 90% SS304L walls as measured by experiments (symbols). The fitted von Mises yield surface, based on uniaxial tension in the longitudinal direction, is shown as a solid line.

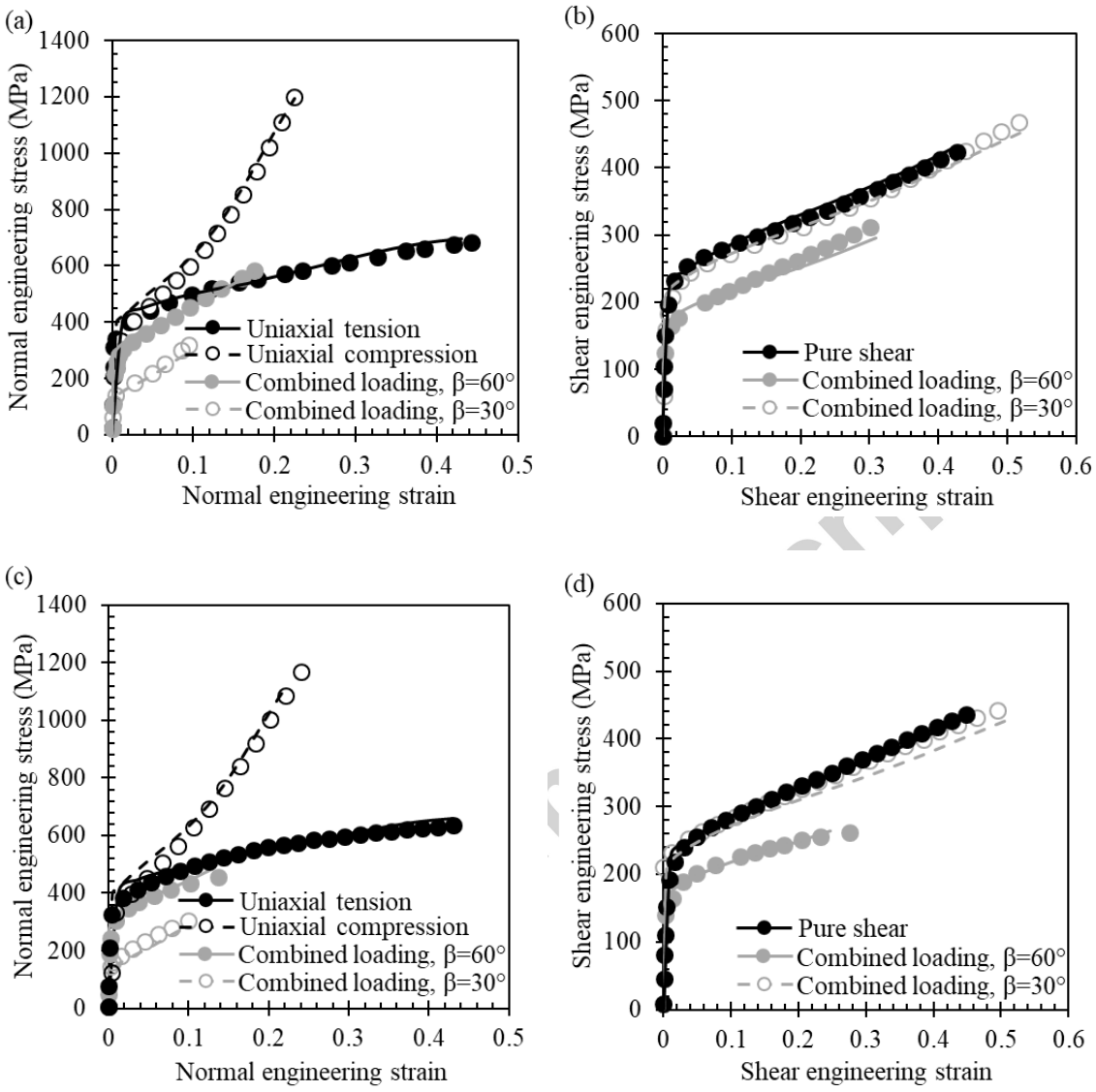

Figure 4. Normal engineering stress-strain curves for specimens under uniaxial tension, uniaxial compression, and combined loading for the (a) 80% SS304L wall and (c) 90% wall. Shear engineering stress-strain curves for specimens under pure shear and combined loading for the (b) 80% SS304L wall and (d) 90% SS304L wall. Symbols correspond to experimental results and lines correspond to results predicted by the calibrated plasticity model. Curves obtained under uniaxial tension, uniaxial compression, and pure shear were used for model calibration and curves under combined loading were used for model validation.

Tables

Table 1. Elemental composition (wt.%) of the pre-alloyed SS304L powder and specimens extracted from the 80% and 90% SS304L walls.

	C	N	Si	Mn	Cr	Ni	Mo
SS304L powder	0.01	0.08	0.50	1.50	19.0	10.3	0.01
80% SS304L	0.01	0.09	0.63	1.27	16.73	9.08	0.05
90% SS304L	0.01	0.09	0.7	1.31	17.05	9.47	0.05

Table 2. Loading conditions of pure shear and combined loading.

	Stress rate in vertical direction	Strain or stress rate in horizontal direction
Pure shear	0 MPa/s	1.3×10^{-4} /s
Combined loading with $\beta = 30^o$	2.1 MPa/s	3.6 MPa/s
Combined loading with $\beta = 60^o$	3.6 MPa/s	2.1 MPa/s

Table 3. Initial values of stress triaxiality, η, and Lode angle parameter, $\bar{\theta}$, for the stress states studied.

	Combined loading with $\beta = 60^o$	Uniaxial tension	Combined loading with $\beta = 30^o$	Pure shear	Uniaxial compression
η	0.38	0.33	0.16	0	-0.33
$\bar{\theta}$	0.85	1	0.46	0	-1

Table 4. Calibrated plasticity model parameters for the 80% and 90% SS304L walls.

	80% SS304L	**90% SS304L**
A **(MPa)**	776.5	776.5
ε_0	0.01	0.01
m	0.55	0.55
k_0 **(MPa)**	384.2	384.2
H_c **(MPa)**	4.5	4.5
c_{max} **(vol.%)**	60	46
n	3.6	3.9
D_0	2.7	2.7
a_η	3.0	3.0
$a_{\theta 1}$	-1.8	-1.8
$a_{\theta 2}$	1.4	1.4
a_W	1.6	1.6

Table 5. Maximum percent difference in stress predicted by simulations compared to experimental results under uniaxial and multiaxial loading.

	Stress state	**Number of samples tested**	**Difference in normal stress (%)**	**Difference in shear stress (%)**
80% SS304L	Uniaxial tension	5	1.7	-
	Uniaxial compression	3	4.9	-
	Pure shear	3	-	1.1
	Combined loading with $\beta = 30^o$	1	7.3	2.6
	Combined loading with $\beta = 60^o$	1	1.9	5.0
90% SS304L	Uniaxial tension	3	4.2	-
	Uniaxial compression	3	3.4	-
	Pure shear	3	-	1.6
	Combined loading with $\beta = 30^o$	1	8.5	6.7
	Combined loading with $\beta = 60^o$	1	9.1	3.0